Renewable and Sustainable Energy Reviews 108 (2019) 380–391

Contents lists available at ScienceDirect

Renewable and Sustainable Energy Reviews

journal homepage: www.elsevier.com/locate/rser

The structural response of a wind turbine under operating conditions with a low-level jet

Walter Gutierrez[a,d,*], Arquimedes Ruiz-Columbie[b], Murat Tutkun[c], Luciano Castillo[d]

[a] Texas Tech University/Department of Mechanical Engineering, 2500 Broadway, Lubbock, TX, 79409, USA
[b] Texas Tech University/National Wind Institute, 2500 Broadway, Lubbock, TX, 79409, USA
[c] Institute for Energy Technology (IFE), P.O. Box 40, NO-2027, Kjeller, Norway
[d] Purdue University/School of Mechanical Engineering, 585 Purdue Mall, West Lafayette, IN, 47907, USA

ARTICLE INFO

Keywords:
Low-level jet
LLJ
Wind energy
Wind turbine
Mechanical response
Azimuthal response

ABSTRACT

Nocturnal low-level jets (LLJs) occurring in the lower layers of the atmosphere are major power resources that play a key role in wind energy production due to their high speed. However, LLJs have also been associated with potential wind turbine damages. Understanding the relation between the incoming wind and the reactions of a wind turbine will help to mitigate the undesirable effects of LLJs, while taking advantage of their intensified energy resource.

High-frequency observational data and NREL FAST code simulations were used to understand the nature of wind turbine reactions to a LLJ. Results indicate that the signal from the incoming wind is detectable in the structural response of the wind turbine at various locations due to interactions with the blades and propagation through the wind turbine components [1]. Characteristic frequencies registered in the LLJ do not dissipate across different parts of the turbine and instead leave measurable footprints.

Azimuth plots of responses at each blade show cardioid-like shapes, with pattern modification observed each time a blade passes by the tower. Presence of the tower breaks the symmetry and influences blade responses to the incoming wind. In certain cases, the cardioid-like shape is lost due to the interaction of tower and blades and a rather irregular pattern is observed.

1. Introduction

The characteristic signature of low-level jets (LLJs) is the presence of relative wind speed maxima usually detected near the top of the stable boundary layer [2], [p. 500]. They are observed when there is stable stratification in the lower atmosphere and cessation of the upward heat flux due to temperature inversion. Detected in many locations around the planet, LLJs are especially important in the Great Plains of the United States, where they contribute to the climate and provide enormous potential for wind energy production. About 75% of LLJs in the region are detected at night, more frequently during the summer season [3].

A previous study [4] demonstrated that LLJs exert a noticeable forcing on wind turbines at altitudes as low as $z \approx 40\,m$ above the ground level. As Fig. 1 shows, heights of current utility-scale wind turbines are well above that altitude, thus placing wind turbines under the frequent impact of LLJs. As reference, the figure shows a representation of the Vestas V164-8.0-MW wind turbine, located in Denmark, whose blade tips reach near 220 m above the ground level. Impacts will be more important in the future as wind turbines continue to increase in height. Therefore, it is critical to understand how the structures of wind turbines are affected in all possible scenarios of LLJs.

LLJs are found to be significant contributors of wind energy due to the wind speed increase in certain conditions and altitudes. Recent studies [4] documented values of wind power density at the height of LLJs peak of about 10–15 times the values observed at the same height but in diurnal unstable conditions occurring a few hours before. This can improve the capacity factor (CF) of a single wind turbine, although the effect over a wind farm is less clear due to the slower wake recovery, which is an expected problem due to the stratification and suppressed vertical velocity fluctuations. A previous study observed that CF increased over 60% during the nocturnal hours, which was attributed to the presence of LLJs [5].

On the other hand, the structural effects must carefully be assessed.

* Corresponding author. Texas Tech University/Department of Mechanical Engineering, 2500 Broadway, Lubbock, TX, 79409, USA.
E-mail addresses: wgutierr@purdue.edu (W. Gutierrez), arquimedes.ruiz-columbie@ttu.edu (A. Ruiz-Columbie), murat.tutkun@ife.no (M. Tutkun), Lcastillo@purdue.edu (L. Castillo).

https://doi.org/10.1016/j.rser.2019.03.058
Received 4 June 2018; Received in revised form 27 March 2019; Accepted 27 March 2019
1364-0321/ © 2019 Published by Elsevier Ltd.

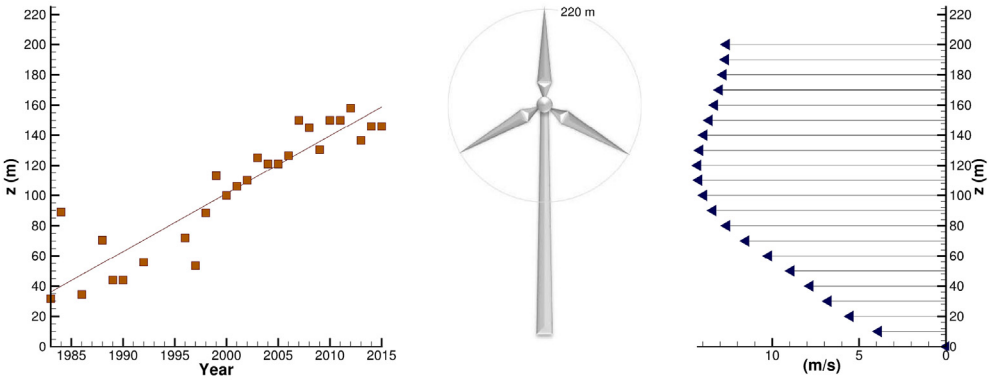

Fig. 1. Trends in utility-scale wind turbine's heights compared with altitudes of LLJs. (a) Trends in wind turbine's heights in the United States, measured from the ground to the tip of the blade in the upper position. (b) Representation of the world's tallest wind turbine (until July 2016), the Vestas V164-8.0-MW located in Denmark. (c) Speed profile of a typical LLJ whose peak occurred at 120 m above the ground level. Figure is adapted from Dr. Walter Gutierrez's Doctoral Dissertation [1].

A major concern to this end is that the significant variation of axial wind speed with height, due to the stronger wind shear, generates an additional moment on the wind turbine [4]. Experimental observations [6,7] demonstrated that mechanical loads and fatigue loads augment when LLJs are present. Moreover, power spectra of the LLJs reveal certain frequencies which sustain themselves across different data sets and those frequencies excite specific modes in the dynamics of wind turbines, thus increasing the probability of structural problems which may lead to permanent deformation and damage [4]. Interestingly, turbine components which are not hit directly by the peak of LLJ exhibit similar frequencies being transmitted unmitigated across the turbine. The reason behind this is not clear and is worth studying in detail. Therefore, the first question concerns the input from the incoming wind and how the footprint sustains across a wind turbine's structure.

The most salient characteristic of a LLJ is a peak of wind velocity, detected at an altitude that is commonly between 100 m and 700 m above the ground level [3]. The wind shear (i.e., wind speed variation with height) changes sign at the jet peak; being positive below the peak and negative above the peak. A previous study demonstrated that the presence of a negative wind shear within the wind turbine's swept area reduces the mechanical loading [8]. Remarkably, this reduction was more pronounced in static parts (i.e., nacelle and tower). By contrast, the presence of negative shears had a very small reduction in forcing on rotating parts (i.e., blades and shafts). It is possible to infer that positive and negative variations in the azimuthal responses can compensate each other as we perform the integration along the entire rotation cycle. Therefore, a second question to address is whether the turbine's responses vary with the rotor's angular position.

Response of the turbine for a given forcing condition is first generated by the interaction between the incoming LLJ and the elements of the structure, specifically the blades and the tower. The loading created by the wind propagates across every part of the turbine, from the tip of the blades to the anchoring point at the base of the tower. Transport of the loads across the turbine is demonstrated by the large correlation between the mechanical responses obtained from adjacent parts of the turbine. The sensor points that are contiguous in the path shown later in Fig. 2 are referenced throughout this article as "neighboring locations."

The first part of this article is dedicated to carefully building an input-output relation between incoming LLJ wind field and different structural components of the wind turbine (e.g., from the blades to the base). The second part of the article explores any dependency exhibited by different elements at different angular position of the blades on the plane of rotation. This insight is useful to understand how the propagation of forcing applied by the incoming wind travels across the turbine. Additionally, it is of interest to characterize the effect of negative shear in the plane of rotation on the structural response of the turbine as a function of the angular positions of the blade.

One should note that a key element in this investigation is the role of the tower, which as a source for perturbation, alters the wind field and breaks the symmetry of the rotor responses. As documented previously [9], a downwind turbine projects a shadow much larger than the shadow projected by an upstream turbine, with a ratio of 5:1. It was also found that the tower clearance does not significantly modify the tower shadow. The geometry of the tower, however, is more relevant, since a streamlined tower reduces the shadow by about 50% compared to a tubular one. The shadow effect is also smaller when a four-legged tower is used. This, on the other hand, leads to more unstable blade responses as a result of interaction of the blades and each leg separately. Thus, it is clear that the presence of a tower produces a complex and asymmetric perturbation on the blades' motions.

This article is organized as follows: Section 2 describes the methods employed in this research. The results are presented in Section 3. The final section 4 consists of discussion and conclusion, with recommendations of future research directions.

2. Methods

The results presented in this paper were obtained following a four-step process. The first step involved measurement of the three components of wind velocity, temperature, pressure and relative humidity from the meteorological tower of the West Texas Mesonet, located at Reese Technology Center near Lubbock, Texas [10]. Datasets received were processed and consolidated into a central database. Then, queries were performed on the database to extract information of past events such as LLJs. In the fourth and final stage, the extracted datasets were used as inflow conditions to compute the mechanical responses of a wind turbine using the aero-elastic simulator FAST. This four-step process was repeated for different conditions to generate a wide dataset to be used in analysis.

2.1. 200-m meteorological tower

The observational data were collected using measurements from the 200-m meteorological tower [10,11], located at $N33°36'27.32''$, $W102°02'45.50''$ and at elevation of 1021 m above sea level. Sensors on tower were installed at 10 altitudes as follows: 0.91 m, 2.44 m, 3.96 m, 10.06 m, 16.76 m, 47.24 m, 74.68 m, 116.43 m, 158.19 m and 199.95 m. All measurements and calculations were performed at a frequency of 50 Hz.

At each vertical position, Gill R3-50 sonic anemometers [12] registered three-components of the instantaneous wind velocity: u (northward - x), v (eastward - y), and w (vertical - z). The vector sum: $\vec{U}_{xy} = \vec{u} + \vec{v}$ represented the instantaneous horizontal wind velocity, normal to the plane of rotation of the turbine rotor, and its modulus was calculated by $U_{xy} = \sqrt{u^2 + v^2}$.

The data received from the tower system were stored in individual files representing blocks of approximately 30-min windows. Those files

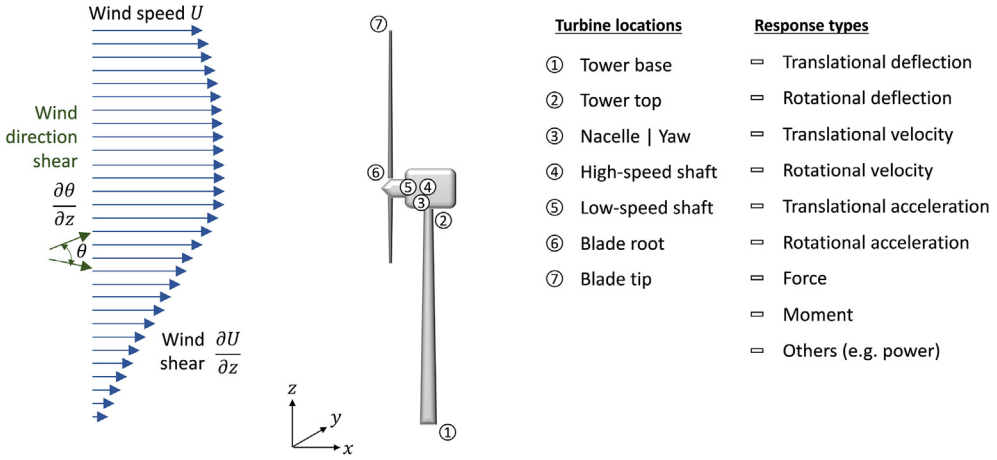

Fig. 2. Locations where wind turbine's responses are measured and response types. The signals from the incoming wind (represented at left in blue) are transmitted across the mechanical responses at each location in the wind turbine, following the path: 7-6-5-4-3-2-1. (For interpretation of the references to color in this figure legend, the reader is referred to the Web version of this article.)

were cleaned of erroneous or incomplete records, before consolidation into a central platform composed of interconnected SQL Server databases. This platform served as a central repository to perform complex queries.

2.2. NREL FAST code for turbine simulation

An experimental setup for the comprehensive study of the interactions between LLJs and wind turbines at different vertical positions would require a complex infrastructure with several wind turbines of different heights, which would make the cost prohibitive. The most reasonable solution is to simulate the turbine's responses using a simulator. The most common software which is used in this type of aeroelastic computations in the United States is the FAST (Fatigue, Aerodynamics, Structures, and Turbulence) code [13], developed by the U.S. National Renewable Energy Laboratory (NREL). Results presented in this article are based on 3-blade wind turbine simulations performed using FAST.

FAST defines at least one coordinate system per interconnection point, resulting in total number of coordinate system to be 13 in a 3-blades wind turbine configuration. They differ from each other on parameters such as origin, movement, angle, and so on. In order to relate responses of the turbine across different parts of the turbine's structure, this document uses simplified noun adjuncts to refer to the three components of those responses, independently of the underlying coordinate system. The labelling convention is shown in Table 1.

2.3. Two-point cross-correlations

To assess how input forcing generated by the wind affects turbine's components, cross-correlations were calculated between compatible responses at neighboring turbine locations, as shown in Fig. 2. For example, the first set of correlations were calculated between the blade tip and the blade root. Each response is a time series of a quantity of interest that is obtained as output from simulations performed using the FAST code. Each time series includes about 30,000 values at the frequency of 50 Hz, which corresponds to a time-lapse of approximately 10 *minutes*. Given the large sample size, the statistical significance is very high and even correlations in the order of the second decimal place can be considered as accurate representation of the underlying process [14]. The tests of statistical significance were verified to be well below the widely used criteria of $p_{value} < 0.05$ [15].

The two-point cross-correlation computations are performed between two output (or response) signals, denoted by $R_A^{(i)}$ and $Q_B^{(j)}$, generated as a result of input signal (or incoming wind). R and Q represent type of response (such as the types listed in Fig. 2), superscripts (i) and (j) indicate direction (such as x, y, and z), and subscripts A and B specify two positions located on a turbine (such as the ones listed in Fig. 2). For example, translational deflection in the streamwise direction at the tip of blade # 1 can be represented as $D_{tip1}^{(x)}$. Table 3 shows some possible correlation combinations. The two-point cross-correlation coefficient, ρ, is written as follows:

$$\rho_{(R_A^{(i)},Q_B^{(j)})} = \frac{E[(R_A^{(i)} - \overline{R_A^{(i)}})(Q_B^{(j)} - \overline{Q_B^{(j)}})]}{\sigma_{R_A^{(i)}}\sigma_{Q_B^{(j)}}} \tag{1}$$

where $R_A^{(i)}$ is the time series of type R at location A and direction (i), and $Q_B^{(j)}$ is the time series of type Q at location B and direction (j). Note that superscripts (i) and (j), and subscripts A and B stand as dummy variables and will be named accordingly depending on the directions and locations of interest. For example, $\rho_{\left(D_{Tip1}^{(x)},F_{Root1}^{(x)}\right)}$ means the correlation is computed between the streamwise (x) translational deflection (D) at the tip of blade # 1 $(Tip1)$ and the streamwise force (F) at the root of blade # 1 $(Root1)$. For a complete list of response symbols, see Table 2. E denotes expected value and the overbar (i.e., $\overline{R_A^{(i)}}$ and $\overline{Q_B^{(j)}}$) indicates time averaging. The standard deviations for corresponding output signals are represented by $\sigma_{R_A^{(i)}}$ and $\sigma_{Q_B^{(j)}}$.

In order to take the propagation time between different locations across the turbine into account, the correlations are computed using a time lag between the two response signals. Hence, we use an updated version of Equation (1) as follows:

Table 1
Wind turbine parameters used for FAST simulations.

Location	Coordinates	Axis	Description
Points in rotating parts such as blades or shafts	Streamwise	x	Positive in the direction of the wind
	Azimuthal	y	Positive in the direction that forms a right-handed coordinate system
	Radial	z	Positive outward
Points in static parts such as nacelle or tower	Streamwise	X	Positive in the direction of the wind
	Spanwise	Y	Positive in the direction that forms a right-handed coordinate system
	Vertical	Z	Positive going away from the ground

Table 2
Nomenclature used for responses in Equation (1) and Equation (2).

General form: $R_A^{(i)} \equiv Type_{Location}^{Axis}$

Parameters	Symbol	Meaning
Types (motions):[a]	*D,d*	Deflection
	V,v	Velocity
	A,a	Acceleration
Types (loads):	*F*	Force
	M	Moment
Locations:	*Tip#*	Tip of blade #
	Root#	Root of blade #
	LSS	Low-speed shaft
	Nac	Nacelle
	TowT	Top of the tower
	TowB	Base of the tower
Axes:	*x*	Streamwise
	y	Azimuthal
	z	Radial
	X	Streamwise
	Y	Spanwise
	Z	Vertical

[a] Uppercase for translational motions, lowercase for rotational motions.

$$\rho_{(R_A^{(i)},Q_B^{(j)},\tau)} = \frac{E\left[(R_A^{(i)} - \overline{R_A^{(i)}})_t (Q_B^{(j)} - \overline{Q_B^{(j)}})_{t+\tau}\right]}{\left(\sigma_{R_A^{(i)}}\right)_t \left(\sigma_{Q_B^{(j)}}\right)_{t+\tau}} \quad (2)$$

where t is time and τ is the time lag between the time series $R_A^{(i)}$ and the time series $Q_B^{(j)}$.

2.4. Dependence on rotor angular position

To calculate the rotor dependence on rotor angular position, a protocol must be established beforehand to define how the rotor's azimuth will be measured. The convention followed is that the rotor position is quantified as the angle or azimuth θ in a polar coordinate system whose center coincides with the rotor hub. The value $\theta = 0$ is defined as the rotor angular position at which the tip of the blade # 1 is at the top. The azimuth θ always coincides with the angular position of the blade # 1 (for characteristic examples, see Fig. 3).

The analysis of the relation between turbine response and rotor azimuth was performed by studying the statistical parameters such as mean, median, and percentiles 2.5%, 16.0%, 84.0% and 97.5%. These parameters allow us to detect whether the rotor position influences the magnitude and stability of the response.

As briefly mentioned in the introduction section, it is of great interest to understand how the presence of negative wind shear within the wind turbine's swept area affects the azimuthal responses. This study follows the parametrization introduced in previous research [8] and uses the turbine-jet relative distance parameter, ξ, to quantify the rotor section impacted by the negative wind shear. The parameter is defined as follows:

$$\xi = \frac{z_t - z_p}{R} \quad (3)$$

where R is the turbine's rotor radius and z_t and z_p are heights above the ground level of the turbine hub and of the LLJ peak, respectively. Characteristic values of ξ are represented in Fig. 4. Note that $\xi = -1$ means that the entire rotor is impacted by positive wind shears. $\xi = 0$ occurs when the rotor section below the turbine hub is impacted by positive wind shears and the upper section by negative wind shears. $\xi = 1$ happens when the entire rotor is impacted by negative wind

Table 3
Cross-correlation coefficients of response signals at neighboring turbine's locations, from Equation (2). For a complete list of symbols, see Table 2.

Between blade tip's motions and blade root's loads			
1	$\rho_{\left(D_{Tip1}^{(x)},F_{Root1}^{(x)}\right)} = 0.899$	$\rho_{\left(D_{Tip1}^{(y)},F_{Root1}^{(y)}\right)} = 0.975$	$\rho_{\left(D_{Tip1}^{(z)},F_{Root1}^{(z)}\right)} = -0.887$
2	$\rho_{\left(d_{Tip1}^{(x)},M_{Root1}^{(x)}\right)} = 0.997$	$\rho_{\left(d_{Tip1}^{(y)},M_{Root1}^{(y)}\right)} = 0.955$	
3	$\rho_{\left(A_{Tip1}^{(x)},F_{Root1}^{(x)}\right)} = 0.628$	$\rho_{\left(A_{Tip1}^{(y)},F_{Root1}^{(y)}\right)} = -0.287$	$\rho_{\left(A_{Tip1}^{(z)},F_{Root1}^{(z)}\right)} = -0.996$
Between blade root's loads and low-speed shaft's loads			
4	$\rho_{\left(F_{Root1}^{(x)},F_{LSS}^{(x)}\right)} = 0.931$	$\rho_{\left(F_{Root1}^{(y)},F_{LSS}^{(y)}\right)} = 0.997$	$\rho_{\left(F_{Root1}^{(z)},F_{LSS}^{(z)}\right)} = -0.064$
Between low-speed shaft's loads and nacelle's loads			
5	$\rho_{\left(F_{LSS}^{(x)},F_{Nac}^{(X)}\right)} = 0.979$	$\rho_{\left(F_{LSS}^{(y)},F_{Nac}^{(Y)}\right)} = 0.012$	$\rho_{\left(F_{LSS}^{(z)},F_{Nac}^{(Z)}\right)} = 0.023$
Between nacelle's motions and tower top's motions			
6	$\rho_{\left(v_{Nac}^{(X)},v_{TowT}^{(X)}\right)} = 1.000$	$\rho_{\left(v_{Nac}^{(Y)},v_{TowT}^{(Y)}\right)} = 1.000$	$\rho_{\left(v_{Nac}^{(Z)},v_{TowT}^{(Z)}\right)} = 0.994$
7	$\rho_{\left(a_{Nac}^{(X)},a_{TowT}^{(X)}\right)} = 1.000$	$\rho_{\left(a_{Nac}^{(Y)},a_{TowT}^{(Y)}\right)} = 1.000$	$\rho_{\left(a_{Nac}^{(Z)},a_{TowT}^{(Z)}\right)} = 0.994$
8	$\rho_{\left(A_{Nac}^{(X)},A_{TowT}^{(X)}\right)} = 1.000$	$\rho_{\left(A_{Nac}^{(Y)},A_{TowT}^{(Y)}\right)} = 1.000$	$\rho_{\left(A_{Nac}^{(Z)},A_{TowT}^{(Z)}\right)} = 0.233$
Between tower top's motions and tower base's loads			
9	$\rho_{\left(D_{TowT}^{(X)},F_{TowB}^{(X)}\right)} = 0.978$	$\rho_{\left(D_{TowT}^{(Y)},F_{TowB}^{(Y)}\right)} = 0.704$	$\rho_{\left(D_{TowT}^{(Z)},F_{TowB}^{(Z)}\right)} = -0.827$
10	$\rho_{\left(d_{TowT}^{(X)},M_{TowB}^{(X)}\right)} = 0.917$	$\rho_{\left(d_{TowT}^{(Y)},M_{TowB}^{(Y)}\right)} = 0.996$	

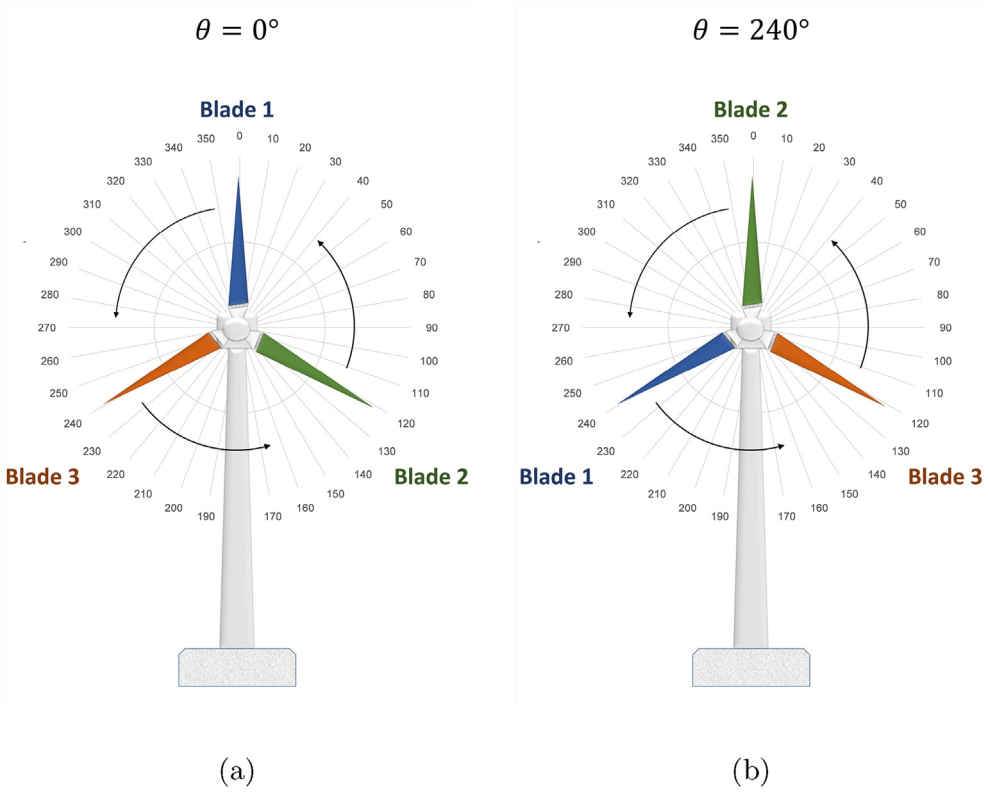

Fig. 3. Characteristic values of the rotor azimuth angle θ. Azimuth θ always coincides with the angle of blade # 1. (a) When $\theta = 0°$, blade # 2 is at 120° and blade # 3 is at 240°. (b) When $\theta = 240°$, blade # 2 is at 0° and blade # 3 is at 120°.

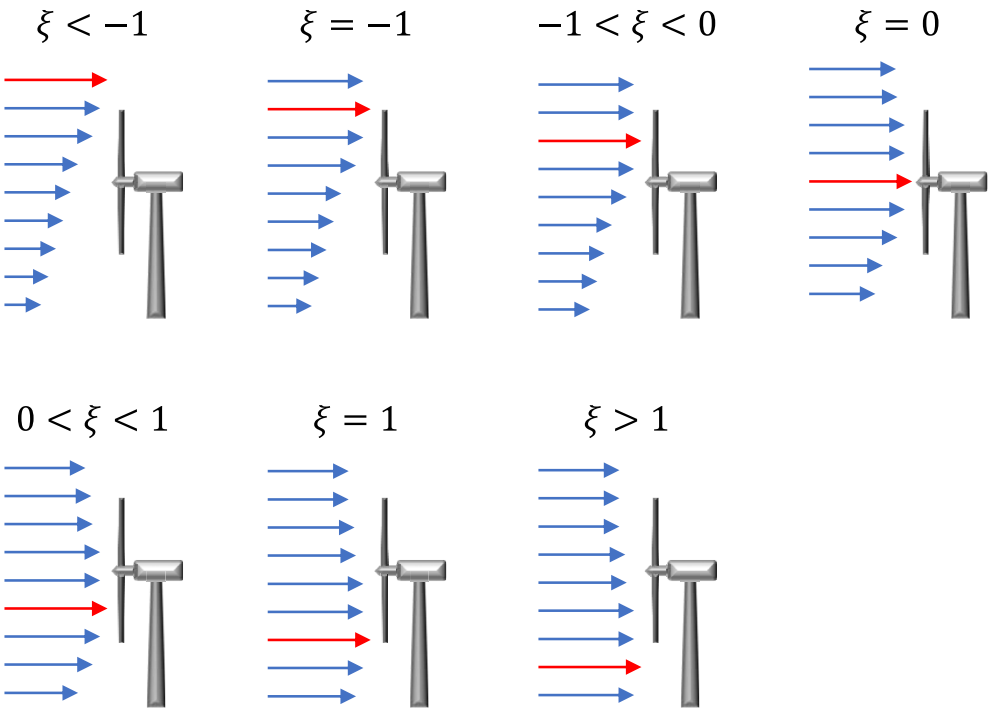

Fig. 4. Characteristic values of the parameter ξ [8]. Blue arrows represent LLJs, with red arrows highlighting the position of their peaks. (For interpretation of the references to color in this figure legend, the reader is referred to the Web version of this article.)

shears.

3. Results

3.1. Correlations between Turbine's parts

Correlations were calculated following the path previously shown in Fig. 2, starting at the tip of the blade and finishing at the base of the tower. Results are summarized in Table 3.

The first three rows of Table 3 reveal that the motions of the tip of the blade were closely followed by corresponding loads at the root. The blade tip deflections (translational and angular) and blade root loads (forces and moments) are strongly correlated as it is evidenced by the high values of correlations seen in rows 1 and 2. The positive correlation between deflections at the tip and loads at the root conforms to the theory approximating the blade geometry to a cantilever beam with uniformly distributed load [16], [pp.34–39]. In that case, the theoretical expressions connecting tip deflections to root shear forces are as follows:

$$d_{Tip}^{(x)} = \frac{q^{(x)}l^4}{8EI} = \frac{F_{Root}^{(x)}l^3}{8EI} \propto F_{Root}^{(x)}$$
$$d_{Tip}^{(y)} = \frac{q^{(y)}l^4}{8EI} = \frac{F_{Root}^{(y)}l^3}{8EI} \propto F_{Root}^{(y)} \quad (4)$$

where $d_{Tip}^{(x)}$ and $d_{Tip}^{(y)}$ are deflections at the blade tip, $F_{Root}^{(x)}$ and $F_{Root}^{(y)}$ are forces at the blade root, $q^{(x)}$ and $q^{(y)}$ are distributed forces along the blade, l is the blade length, E is the blade's modulus of elasticity, and I is the blade's moment of inertia. The correlations observed were actually slightly less than 1.0 due to the presence of some accelerations and also because the geometry of the blade actually bulged slightly under the applied wind forces.

The correlations are greater as the time lag is considered. As noticed in Fig. 5, maximum correlations between blade tip translational deflections and blade root forces in the streamwise, azimuthal, and radial directions took place at time lags of $5/50\,s$, $5/50\,s$, and $3/50\,s$, respectively. This delay can be attributed to the long length of the blade (approximately $35\,m$). For the same reason, maximum correlations between blade tip angular deflections and blade root moments around the streamwise direction, and around the azimuthal direction occurred at time lags of $5/50\,s$ and $6/50\,s$, respectively (not shown). The cyclical pattern observed in Fig. 5 (b) is attributed to back-and-forth fluctuations of the azimuthal tip deflection, with a period of about $1\,s$.

On the other hand, the correlations of the blade root forces and the blade tip accelerations (seen in Table 3, row 3), although significant, were not as high as with deflections, which leads to infer that the correlations with accelerations existed but were not connected to a linear model. Time integration of tip acceleration A gives tip velocity V, and integration of tip velocity gives tip deflection D. The three signals are not in phase, e.g., if $A = 0$, then $V = const.$, and if $V = const. \neq 0$, then $D = Vt$. Thus, tip accelerations and tip deflections are not in phase. We also know, from row 1 of Table 3, that $\rho_{\left(D_{Tip1}^{(x)}, F_{Root1}^{(x)}\right)}$ is high but not 1 (same analysis can be performed in the y-axis). Thus, we can say that $\rho_{(A_{Tip1}^{(x)}, F_{Root1}^{(x)})} \neq \rho_{(D_{Tip1}^{(x)}, F_{Root1}^{(x)})}$, but it is not possible to say yet which one should be greater.

To find it out, we can accept that the ideal model of the blade is the cantilever, which establishes a linear relation between tip deflections and root forces. In this ideal model, $\rho_{\left(D_{Tip1}^{(x)}, F_{Root1}^{(x)}\right)} = 1$. In reality, $\rho_{\left(D_{Tip1}^{(x)}, F_{Root1}^{(x)}\right)} < 1$, as shown in Table 3, but nevertheless this would be the best correlation between any of the three signal types A, V, or D at the tip and F at the root. Therefore, the expected result is $\rho_{\left(A_{Tip1}^{(x)}, F_{Root1}^{(x)}\right)} < \rho_{\left(D_{Tip1}^{(x)}, F_{Root1}^{(x)}\right)}$.

From the blade root, the signals propagate further into the low-speed shaft. The numbers in row 4 of Table 3 reveal that strong correlations existed between the forces at both locations in the streamwise and azimuthal directions, which point out an equilibrium of forces. The exception occurred in the axial direction with an apparent disconnection between both parts' responses. This can be attributed to very low magnitudes of the axial forces, which make the signal transmission non-significant in presence of the dampening effect of the connecting coupling.

From the low-speed shaft, the signals were transmitted to the nacelle and the top of the tower. Row 5 of Table 3 indicates a strong correlation between forces in the streamwise direction, coinciding with the direction of the thrust force. On the other hand, y- and z-components appear to be uncorrelated. In fact, there are two coordinate systems used in this configuration; a fixed one used to describe the static components (i.e., nacelle and tower), and a rotating one used for rotating components (i.e., blades and shafts). While this does not affect the comparison of components in the x-axis, one should not compare the components in the y- and z-axis directly in this framework.

Correlation coefficient values presented in rows 6, 7 and 8 of Table 3 reveal that motions of the nacelle were strongly correlated with the motions of the top of the tower. The strong coupling can be attributed to the close proximity of the turbine parts in this case. The only exception is the translational accelerations in vertical direction; however, it should be noted that value of the correlation coefficient significantly increased when the time lag was taken into account. A rather low correlation of this component can be explained by the magnitude of the vertical accelerations, which is low and makes the signal transmission more susceptible to the dampening effect of the coupling between nacelle and tower.

Finally, rows 9 and 10 of Table 3 demonstrate that the motions at the tower's top were strongly correlated with the corresponding loads at the tower's base. As with the blades, the tower can be approximated to a cantilever model, which explains the linear relation between deflections at the top end and loads at the bottom end.

According to the data presented in Table 3, the turbine exhibits a large degree of cohesion in front of the external loads applied. The system is primarily excited through the wind-facing elements (i.e. the blades) and then the motions and loads are transported across the whole structure until they are finally absorbed at the point of anchoring to the ground (i.e., the tower's base).

3.2. Response signals at the blade: cardioid behavior

This study also investigated how the turbine's responses varied with the rotor azimuthal position. Fig. 6 shows the azimuthal responses corresponding to the deflections of the tip of each blade in the azimuthal direction, at $\xi = 0$. The most remarkable feature observed is the lack of axial symmetry. This defies the apparent expectation of a circular pattern. The LLJ's wind speed fluctuations were negligibly small so that it can be considered constant in the timespan of the measurement, leading to time scales much larger than the scales defined by the turbine's rotation. Therefore, the lack of symmetry cannot be explained by variations in the incoming LLJ's wind speed, which were very small.

A more plausible explanation is the uneven action of the blade weight, which acts to compensate the rotation-induced bending at one side to create a minimum (e.g. at 90° in the plot of blade 1), and adds more bending at the other side to create a maximum (e.g. at 270° in the plot of blade 1). As a result, cardioid-like responses are observed in each plot. It can also be noticed that the plots of the three blades converged to almost identical shapes, which only differed by the angle at which they are rotated with respect to the polar coordinate system. When the three signals are combined into the shaft, they should produce a radially-symmetric response.

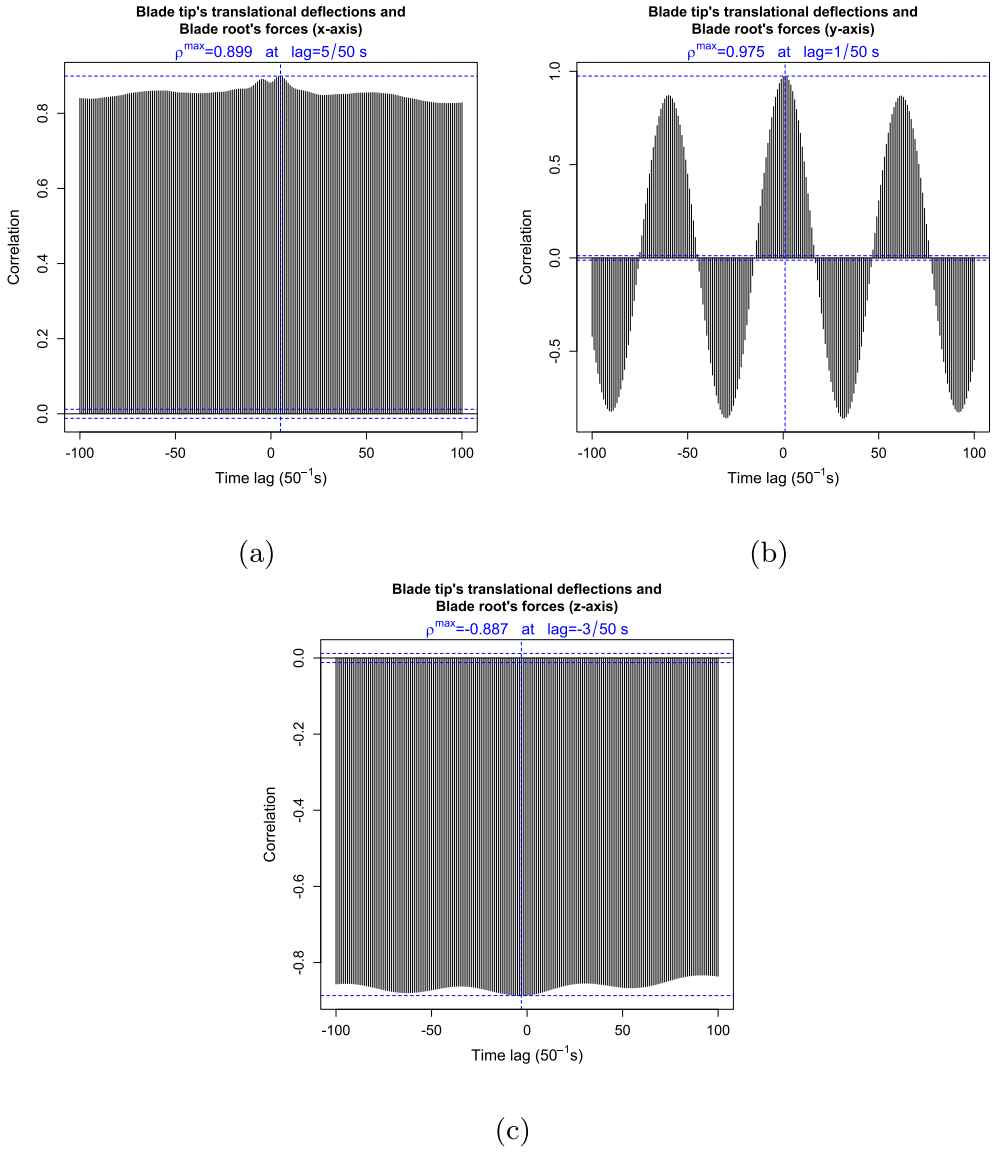

Fig. 5. Time-lag correlations between blade translational deflections and blade root forces. Dashed lines cross at points where global maximum correlations are found. Those values are shown in blue color. (a) Streamwise direction. (b) Azimuthal direction. (c) Radial direction. (For interpretation of the references to color in this figure legend, the reader is referred to the Web version of this article.)

3.3. Response signals at the blade: non-cardioid behavior

Fig. 7 shows the azimuthal responses corresponding to the deflections of the tip of each blade in the streamwise direction, at $\xi = 0$. Lack of symmetry is more apparent than in the case observed earlier and presented in Fig. 6.

This behavior can be attributed to the cycling of the blades across uneven wind shears in the lower and upper sections of the turbine swept area. This factor, however, should produce smooth changes in the plots and can hardly explain the sudden variation of deflection that is observed in the plots at the angles between 30° and 60°. On the other hand, it should be noticed that each time the blade # 1 passes through this arc, the blade # 3 crosses in front of the tower, which implies the modification of the wind field around the tower, disturbing the aerodynamics in the neighboring zone. The plots in Fig. 8 show an increase in the streamwise deflection when the blade approaches the tower, which indicates acceleration of the flow in the strait between the tower and the blade. The Bernoulli equation can be used to explain and support this argument:

$$P + \frac{1}{2}\rho v^2 + \rho g z = constant \tag{5}$$

where P is pressure, ρ is density, g is gravity, and z is height. Omitting the impact of any variation of z, the emergence of a narrow decreases the area; therefore, v augments and P decreases, creating a suction that may bend the blade further.

Based on Fig. 7, the streamwise deflection evolution throughout one complete rotor revolution may be described as follows: As observed in the plots, at azimuths around 30° to 40° the blade deflection started to increase, pulled by the tower-induced suction. The deflection reached maximum values at 180°, i.e., when the blade was exactly in front of the tower. The median values receded shortly after, reaching minima that depended on ξ. For $\xi = -1$ and $\xi = 0$, those minima occurred within approximately the same interval of 320° to 30°. For $\xi = 1$, the minima occurred sooner, in the arc 250° to 330° (as shown in Fig. 10 in the next section).

The plots reveal an interesting anomaly in the arc between 30° and 60°. This abrupt decrease in mean values can be attributed to the aerodynamics changes induced by the tower and the modification of the pressure field. When the blade approached this arc with deflections

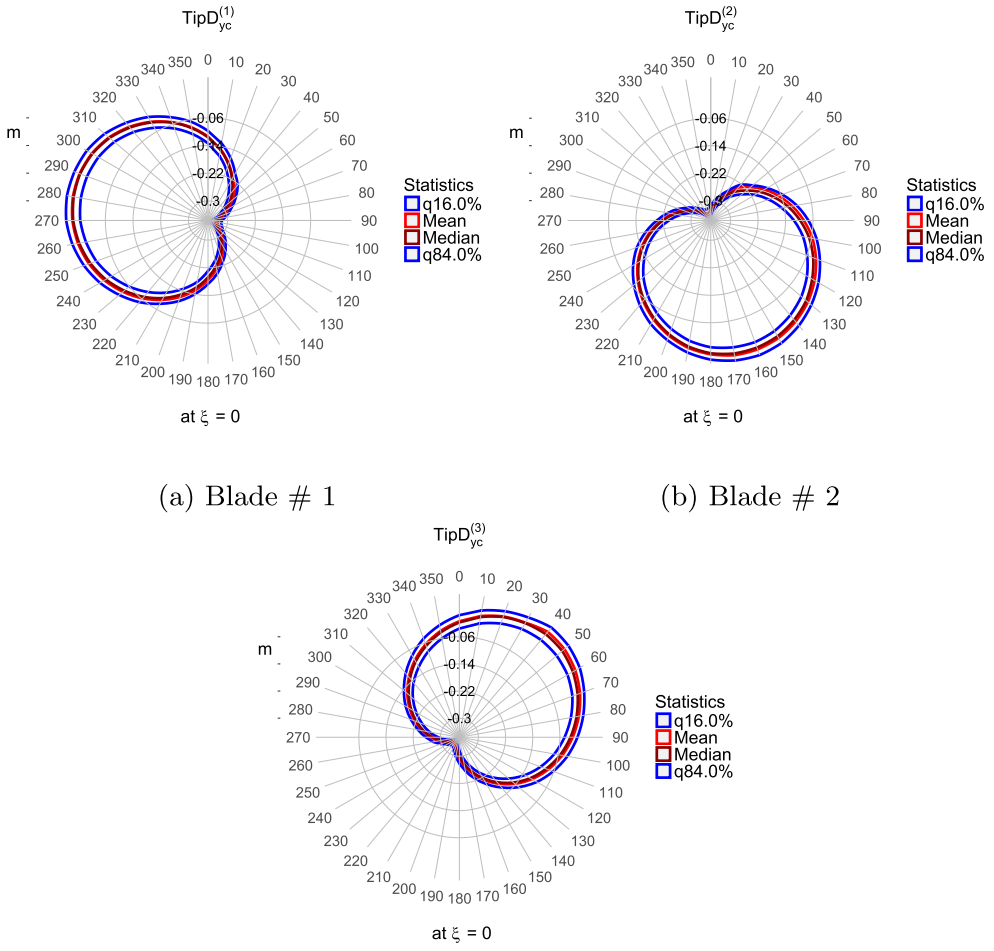

Fig. 6. Variation with rotor azimuth of the blades tip's deflection in the azimuthal direction. In each subfigure, the zero-angle position coincides with that rotor position in which the blade # 1 is exactly pointing upward. The red lines connect mean values, the brown lines connect median values, and the pairs of blue lines enclose the regions where 68% of the values are found. (For interpretation of the references to color in this figure legend, the reader is referred to the Web version of this article.)

lower than usual, it might have experienced high-pressure that pushed the blade away from the tower.

As shown, each blade reached equilibrium individually (meaning the time when azimuthal behaviors started repeating from one cycle to another); however, those equilibrium patterns were different between blades, resulting in the three subfigures showing different patterns. Our hypothesis connects this to the perturbation in the wind field created when one of the blades started crossing in front of the tower. This perturbation affected significantly the entry conditions that the next blade encountered when it was its turn to pass in front of the tower. As a result, each blade faced different wind fields in the section around the tower and consequently generated different motions and loads that were propagated across the turbine structure. A cycle-to-cycle equilibrium was ultimately reached, but this equilibrium was individual for each blade and not equal between them. As a result, peaks and sinks in the blade signals did not compensate each other into a smooth combined signal at the shaft. Therefore, the superimposition of the three signals into a common response at the shaft was not radially-symmetric. This may explain why some effects (e.g., the dampening effects of the negative shears) are amplified when the signals reach the static parts of the turbine.

Fig. 8(a) shows the plot corresponding to blade # 1 with percentiles 16.0% and 84.0% (zoomed-in view), while Fig. 8(b) also adds percentiles 2.5% and 97.5% (zoomed-out view). The figure reveals that this region was narrower in the arc between 330° and 30°, which means that the signal was more stable in the upper positions. At 30° the variance increased abruptly, which may indicate that the blade hit the perturbation wave created by the interaction between the tower and the preceding blade.

3.4. Resulting responses at the tower base

Fig. 9 displays the azimuthal responses of three components of the force at the tower base. As predicted, the three non-cardioid-like streamwise signals from the blades do not compensate each other, in particular the peaks and the sinks; therefore, the streamwise bending force response at the tower base (seen at the figure left) appears asymmetrical. The anomaly at 30° is clearly observed and can certainly lead to an added source of fatigue.

The spanwise response, seen also in Fig. 9, was inherited from the superimposition of the three cardioid-like streamwise signals at the blades (with input from the weaker axial signals). As predicted, the resulting response is almost axially-symmetric. Moreover, the resulting pattern is almost circular. An interesting pattern is observed for the vertical component shown as the last sub-plot in Fig. 9, which also was inherited from the streamwise and the axial blades' signals. The

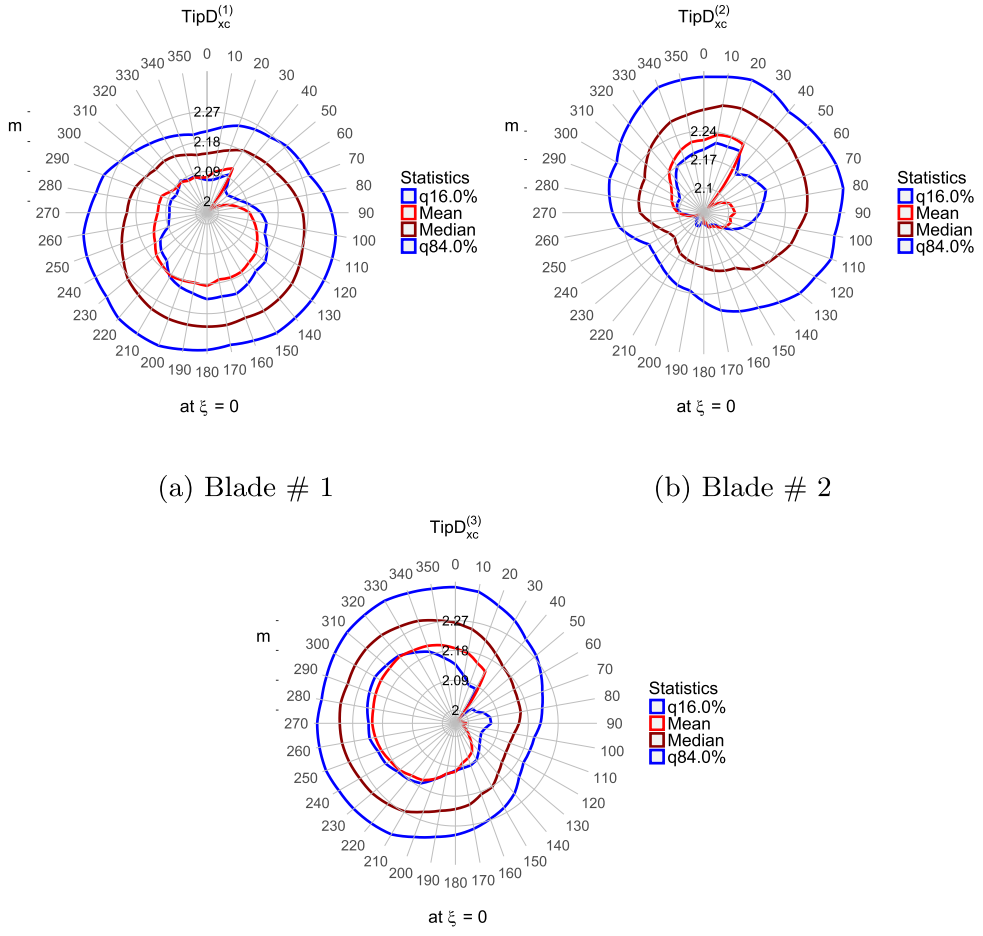

Fig. 7. Variation with rotor azimuth of the blades tip's deflection in the streamwise direction. In each subfigure, the zero-angle position coincides with that rotor position in which the blade # 1 is exactly pointing upward. The red lines connect mean values, the brown lines connect median values, and the pairs of blue lines enclose the regions where 68% of the values are found. (For interpretation of the references to color in this figure legend, the reader is referred to the Web version of this article.)

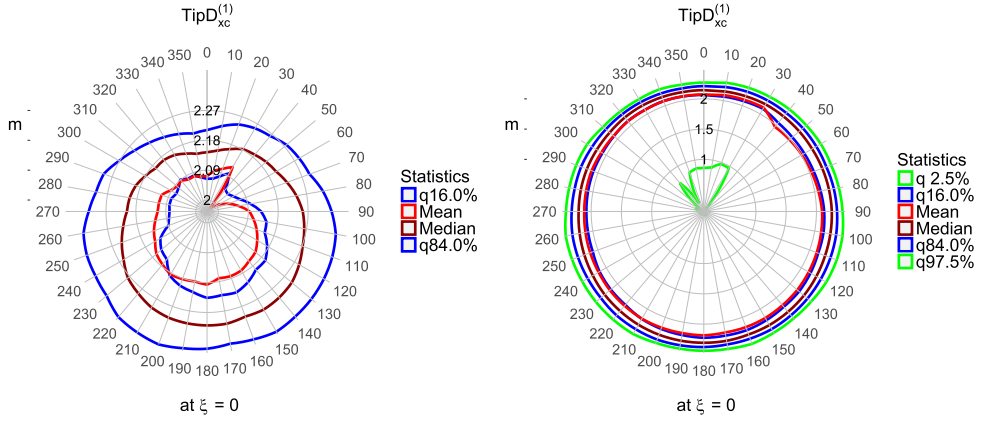

Fig. 8. Zoom-in and zoom-out views of the variation with rotor azimuth of the tip's deflection of blade # 1 in the streamwise direction. The zoomed-out view (at right) adds an extra pair of percentiles (in light green) that encloses 95% of the values. (For interpretation of the references to color in this figure legend, the reader is referred to the Web version of this article.)

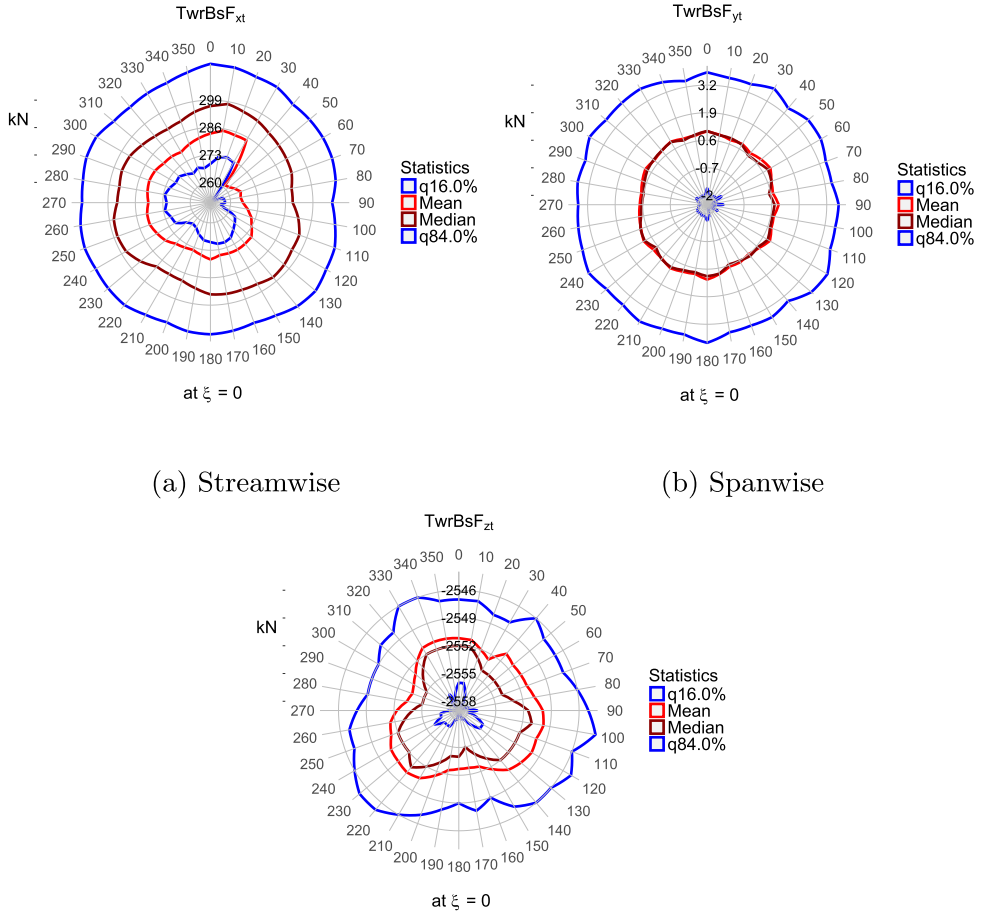

Fig. 9. Variation with rotor azimuth of the tower base's forces. In each subfigure, the zero-angle position coincides with that rotor position in which the blade # 1 is exactly pointing upward. The red lines connect mean values, the brown lines connect median values, and the pairs of blue lines enclose the regions where 68% of the values are found. (For interpretation of the references to color in this figure legend, the reader is referred to the Web version of this article.)

response is almost axially-symmetric, but not circular. It should be noticed that the compression force at the tower is much stronger than the two bending components because it is supporting the weight of the structure. Therefore, it is inertially more resilient to the excitation of the incoming signal from the blades.

3.5. Variations in the azimuthal responses with the presence of negative wind shear

Finally, it is of interest to know how these azimuthal responses were affected by the presence of negative shears, represented by the parameter ξ. Fig. 10 shows the results corresponding to the deflection of the tip of the blade # 1 in the streamwise direction. The top row shows results at $\xi = -1$, which is the simulation case where the turbine rotor was entirely impacted by positive wind shears. The simulation with $\xi = 0$ is seen in the middle row, representing the case with the peak of the jet impacting exactly at the turbine's hub height. Finally, results from the simulation with $\xi = 1$ are displayed in the bottom row, indicating the case with negative wind shears impacting the totality of the turbine's rotor. At each row, the left column presents four percentiles ($q2.5$ %, $q16.0$ %, $q84.0$ %, and $q97.5$ %) and the right column shows only two percentiles ($q16.0$ % and $q84.0$ %) to provide a zoom into the region of the inner percentiles.

Although the integral of the response seems to be similar for the three cases, the shape of the statistical response is flattened for the case $\xi = 1$, resulting in minima occurring sooner at around 250° to 330°. Considering that the blade is the main point of entry of the wind signal inside the wind turbine's structure, this behavior may explain the stronger influence of the parameter ξ on the static parts. The rather constant integral of the response may explain the small impact that the presence of negative shears has on the blades and other rotating parts. On the other hand, the peaks and sinks in the azimuthal profile for $\xi = 1$ do not translate strongly into the responses in the static parts; therefore, the integrated responses are not necessarily azimuthally constant.

4. Discussions and conclusions

The footprint of the incoming wind was detected in the wind turbines responses due to the interactions of different components with the turbine blades. Some of the blade responses converged to a cardioid-like shape in the azimuthal plot due to the combination with the weight forces. Those responses reached global equilibrium after a certain number of rotations, i.e., the azimuthal shape of the responses in the three blades converged to an approximately common pattern. After combined, the resulting responses were basically radially-symmetric.

On the other hand, other response components did not converge to a single pattern for the three blades, suggesting that each blade may have found different wind field states as they entered into the tower-induced perturbation field, thus converging to individual patterns. As the incoming wind speed was almost constant during the timeframe of the

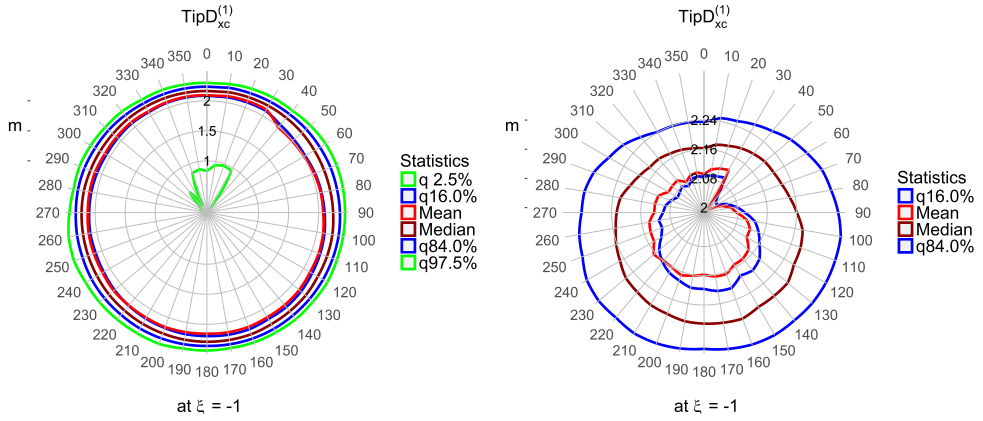

(a) $\xi = -1$, zoomed-out (b) $\xi = -1$, zoomed-in

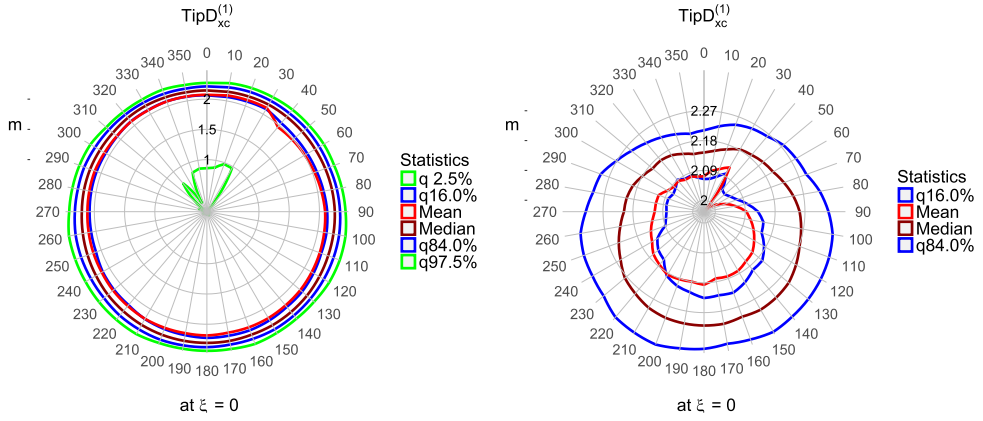

(c) $\xi = 0$, zoomed-out (d) $\xi = 0$, zoomed-in

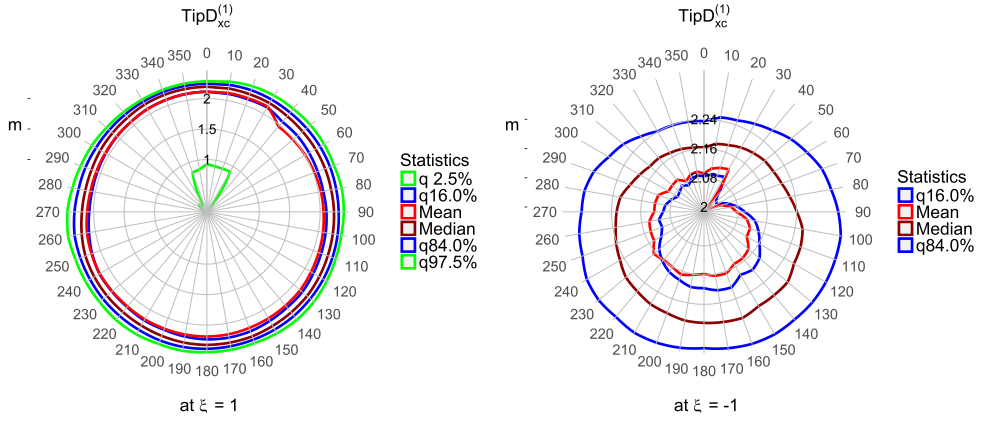

(e) $\xi = 1$, zoomed-out (f) $\xi = 1$, zoomed-in

Fig. 10. Variation with rotor azimuth of the blade tip's deflection in the streamwise direction for different values of ξ. Rows, from top to bottom, represent results at $\xi = -1$, $\xi = 0$, and $\xi = 1$ respectively. Subfigures at right are zoomed-in views of the subfigures at left.

sample (10 min), this behavior seems to indicate that the initial state was very important for the future history. The first blade crossing in front of the tower perturbed the wind field around the tower and created different entry conditions for the next blade passing in front of the tower. As a result, the perturbation generated by the second blade was different and, as a result of this, the entry conditions for the third blade were also different. The process repeated during the whole simulation timeline.

In cardioid-like responses, the three blade signals finally converged to a single pattern after enough rotor revolutions. The global convergence can be defined as the state reached when the signal at each individual blade is equal from one rotor revolution to another one in the future, and also when the signals at the three blades are equal in the same rotor revolution. In non-cardioid-like responses, however, this global convergence was not reached in the timeframe of the sample. They seem to have reached what can be defined as local convergence, in which the signal at each individual blade was equal from one rotor revolution to another one in the future, but the signals at the three blades were not equal in the same rotor revolution.

The signals from the three blades combined to form the responses at

the low-speed shaft which in the globally-converging cases were radially-symmetric. The signals then propagated through the parts of the wind turbine structure until reaching the point of anchoring to the ground at the base of the tower. This seemingly perfect transmission may explain why some features of the energy spectra, such as characteristic frequencies, are found to survive in the responses of rather distant turbine parts.

Some blade responses converged to cardioid-like shapes in an azimuth plot due to the combined effect of the rotation-induced deflections and the weight-induced deflections. For those responses, global equilibrium was reached after enough rotations, i.e., the azimuthal shape of the response components of the three blades converged to an approximately common pattern. On the other hand, statistical analysis of the output response from some of the components did not converge to a single pattern for the three blades, suggesting that each blade found a different wind field when they entered into the tower-induced perturbation field, thus converging to individual patterns.

Future research may investigate whether the convergence of some signals to different patterns for each blade can be the result of each blade finding different wind fields as they enter into the tower-induced perturbation. Future research may also assess experimentally the hypothesis of the connection between the tower-blade interactions and the low-frequency noise that propagates long distances from the wind turbine. If successful, measures to reduce or eliminate the noise will certainly remove one of the main concerns for the acceptance of the wind energy.

Declarations of interest

None.

Funding

This work was supported by the National Science Foundation [grant numbers NSF-CBET #1157246, NSF-CMMI #1100948, and NSF-OISE-#1243482].

References

[1] Gutierrez Rodriguez W. Numerical analysis of the interactions between low-level jets and wind turbines and its impact on performance, power production and mechanical responses Doctoral dissertation Lubbock, Texas, USA: Texas Tech University; 2017

[2] Stull RB. An introduction to boundary layer meteorology vol. 13. Springer Science & Business Media; 1988. https://doi.org/10.1007/978-94-009-3027-8.

[3] Stensrud DJ. Importance of low-level jets to climate: a review. J Clim 1996;9:1698–711.

[4] W. Gutierrez, G. Araya, P. Kiliyanpilakkil, A. Ruiz-Columbie, M. Tutkun, L. Castillo, Structural impact assessment of low level jets over wind turbines, J Renew Sustain Energy 8 (2). https://doi.org/10.1063/1.4945359. URL http://scitation.aip.org/content/aip/journal/jrse/8/2/10.1063/1.4945359.

[5] Wilczak J, Finley C, Freedman J, Cline J, Bianco L, Olson J, Djalalova I, Sheridan L, Ahlstrom M, Manobianco J, Zack J, Carley JR, Benjamin S, Coulter R, Berg LK, Mirocha J, Clawson K, Natenberg E, Marquis M. The wind forecast improvement project (WFIP): a public-private partnership addressing wind energy forecast needs. Bull Am Meteorol Soc 2015;96(10):1699–718. https://doi.org/10.1175/BAMS-D-14-00107.1.

[6] Kelley N, Shirazi M, Jager D, Wilde S, Adams J, Buhl M, Sullivan P, Patton E. Lamar low-level jet project interim report, Interim Report NREL/TP-500-34593. Golden, Colorado, USA: National Renewable Energy Laboratory (NREL); 2004.

[7] Kelley ND. Turbulence-turbine interaction: the basis for the development of the TurbSim stochastic simulator. Golden, Colorado, USA: National Renewable Energy Laboratory (NREL); 2011. Tech. Rep. NREL/TP-5000-52353.

[8] Gutierrez W, Ruiz-Columbie A, Tutkun M, Castillo L. Impacts of the low-level jet's negative wind shear on the wind turbine. Wind Energy Sci 2017;2(2):533–45. https://doi.org/10.5194/wes-2-533-2017https://www.wind-energ-sci.net/2/533/2017/.

[9] Zahle F, Aagaard Madsen H, Srensen NN. Research in aeroelasticity EFP-2007-II, danmarks Tekniske universitet, ris nationallaboratoriet for bredygtig energi, Roskilde, Denmark. 2009. p. 11–29. Ch. Evaluation of tower shadow effects on various wind turbine concepts, paper no. Ris-R-1698(EN). URL orbit.dtu.dk.

[10] West Texas Mesonet. Site information. January 2017http://www.mesonet.ttu.edu/, Accessed date: 23 February 2017.

[11] Hirth B, Schroeder J. A summary of the national wind institute meteorological measurement facilities at the Texas tech university's reese technology center field site Lubbock, Texas, USA: National Wind Institute; 2014. Report.

[12] Gill Instruments Limited. Omnidirectional (R3-50) ultrasonic anemometer. 2005. Lymington, Hampshire. UK.

[13] NREL National Wind Technology Center. NWTC information portal (FAST v8). July 2016https://nwtc.nrel.gov/FAST8, Accessed date: 26 February 2016.

[14] Udovii M, Badari K, Bili-Zulle L, Petroveki M. What we need to know when calculating the coefficient of correlation? Biochem Med 2007;17(1):10–5. https://doi.org/10.11613/BM.2007.002.

[15] Fisher RA. Breakthroughs in statistics. Springer series in statistics (perspectives in statistics). New York, NY, United States: Springer; 1992. p. 66–70. https://doi.org/10.1007/978-1-4612-4380-9_6. Ch. Statistical methods for research workers.

[16] Timoshenko S, Goodier JN. Theory of elasticity. third ed. New York - Toronto - London: McGraw-Hill Book Company, Inc.; 1951.